



 Cite this: *RSC Adv.*, 2020, 10, 7092

N-Substitution of acridone with electron-donating groups: crystal packing, intramolecular charge transfer and tuneable aggregation induced emission†

 Renfei Liu, Guanxing Zhu and Gang Zhang *

Acridone derivatives with electron-rich triphenylamine functionalized at the amino position were synthesized and their properties were experimentally and computationally investigated. The single crystal structure analysis revealed that the π - π interaction of acridone and the formation of hydrogen bonds of carbonyl and the hydrogen atoms of the pending phenyl ring were crucial in the determination of molecular packing in the crystalline state. An intramolecular charge transfer (ICT) process was observed between acridone and triphenylamine even with reduced conjugation by the nitrogen atom of acridone. Tuneable aggregation induced emissions with blue and green fluorescence were found due to the different aggregation state and particle size, which varied according to the water content in THF. Furthermore, the size of the spacer between acridone and the appended amine was also important in adjusting the property of aggregation induced emission or aggregation caused quenching in the solid state.

Received 17th December 2019

Accepted 12th February 2020

DOI: 10.1039/c9ra10615d

rsc.li/rsc-advances

Introduction

Acridone is a basic structural unit of natural alkaloids, which has received considerable attention for its good bioactivity.¹ The tricyclic acridone contains an electron-donating amine and an electron-withdrawing carbonyl in the central ring and demonstrates excellent photoluminescence and wonderful photostability,² which makes it a good fluorescence signalling unit in sensors.^{3–7} Various organic functional materials with interesting properties have been prepared by the functionalization of acridone at the positions of the amine, carbonyl and the phenyl ring. The connection of functional groups to the phenyl ring of acridone is among the most studied owing to the ready halogenation followed by the well-developed cross-coupling reactions. For example, the introduction of amine or carbazole to the phenyl ring of acridone would give hole-transporting materials or host materials for OLED applications.^{8–12} The acridone units could also couple with each other at the phenyl ring to form acridone oligomers with tuneable energy levels.¹³ The functionalization of carbonyl of acridone usually involved the formation of C–C double bonds with another functional group, such as malononitrile, or fluorene, to furnish molecules with variable colour upon external

stimuli due to the conformational change.^{14–16} The introduction of biphenyl carbazole or tetraphenylethylene to the amino position of acridone can also supply molecules with interesting electroluminescence and piezochromic luminescence properties.^{17–19}

Molecules containing electron-donating groups and electron-withdrawing groups in the chain can form a donor–acceptor system with lower energy gaps and are good candidates as photoelectric materials or as fluorescence dyes for bioimaging.^{20–24} When acridone is used to construct a donor–acceptor system, it can serve as an acceptor once the electron-donating groups are linked to the phenyl ring to ensure an efficient ICT process through the phenyl ring to the carbonyl.¹² The condensation of carbonyl of acridone and cyanoacetic esters can also generate an acridone based donor–acceptor system, which lowers the rotational barrier with controllable rotational rate around the formal C–C double bond.²⁵ Recently we found that acridone can be used as a donor when the electron-withdrawing anthraquinone was connected to the amino position of acridone to generate a molecule with interesting thermally activated delayed fluorescence properties.²⁶ However, the presence of a nitrogen atom in acridone makes it difficult to build a donor–acceptor system with acridone as an acceptor *via* N-substitution due to the reduced conjugation. To further study the influence of N-substitution on the properties of acridone, herein we report the synthesis and properties of electron-rich triphenylamine functionalized acridone at the amino position. For a purpose of comparison, the N-substitution of acridone with methoxyphenyl is also involved.

Co-Innovation Center for Efficient Processing and Utilization of Forest Products, College of Chemical Engineering, Nanjing Forestry University, Nanjing, 210037, P. R. China. E-mail: gangzhang@njfu.edu.cn

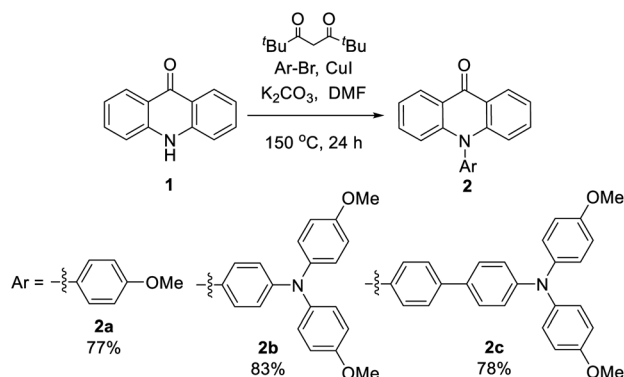
† Electronic supplementary information (ESI) available. CCDC 1972073–1972075. For ESI and crystallographic data in CIF or other electronic format see DOI: 10.1039/c9ra10615d



Results and discussion

The synthesis of *N*-substituted acridone derivatives could be easily achieved *via* copper-catalyzed Ullmann amination of acridone and the related aryl bromide with 2,2,6,6-tetramethylheptane-3,5-dione as ligand to give the target compounds in 77–83% yields (Scheme 1).²² All the compounds were fully characterized by NMR, IR and HRMS.

Single crystals that are suitable for X-ray diffraction analysis were obtained by slow evaporation of ethanol/dichloromethane solution (**2a** and **2b**) or vapor diffusion of hexane into the toluene solution (**2c**), which allows a detailed structural investigation on the conjugation and intermolecular interactions in the solid state (Fig. 1). In the acridone moiety of these three compounds, the shortest C–C bonds with the distances 1.36–1.37 Å are found at the *a* and *c* positions, indicating the largest olefin character. Meanwhile, the bond length of carbonyl is 1.24 Å, which is longer than that of the relevant C–O double bond. The bond alternation indicates the presence of ICT process in acridone, as verified in other reports.^{13,26} The C–N bond between acridone and the pending phenyl has a length of 1.45 Å. The dihedral angles of the acridone plane and the pending phenyl ring are in the range 75–85° due to the steric hinderance. The bond lengths and dihedral angles are in good agreement with those of the non-substituted *N*-phenylacridone.²⁷ The dihedral angles in the triphenylamine moiety of **2b** and **2c** are in the range 63–82°. The dihedral angle of the two methoxyphenyl rings is larger than the other ones around the nitrogen atom. It is worth mentioning that the three N–C bond lengths are different at the triphenylamine moiety with the shortest one (1.41 Å) at the pending phenyl that connects to the acridone, while the other two are slightly longer with the distances 1.42–1.43 Å. The bond length difference demonstrated the delocalization of electron from the triphenylamine towards the acridone unit. The crystal analysis also revealed the π – π interactions between the acridone moiety with the distances 3.42–3.61 Å. The hydrogen bonds between the oxygen atom of carbonyl and the hydrogen atom of pending phenyl ring with the distances in the scale 2.30–2.58 Å are all observed in these crystal structures. The \angle C–H \cdots O angles are 140–169°. These



Scheme 1 Synthesis of acridone derivatives with electron rich groups at the amino position.

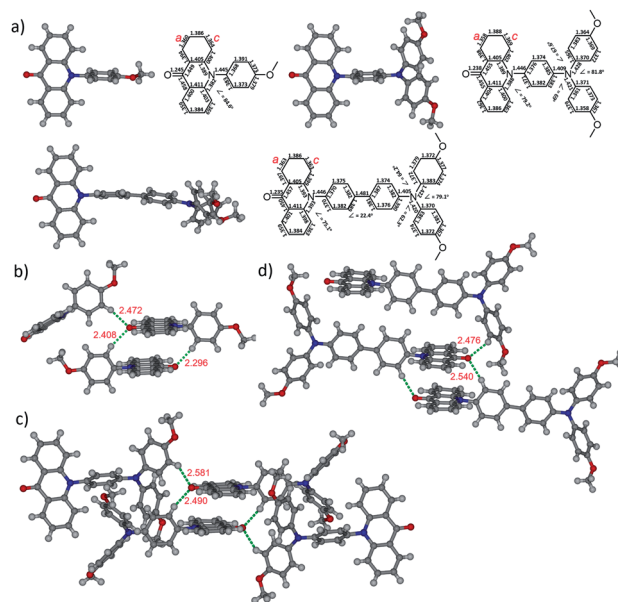


Fig. 1 Crystal structures of **2a**–**2c**. (a) Crystal structural information; crystal packing and hydrogen bond lengths around carbonyl (b) **2a**, (c) **2b** and (d) **2c**.

informations of hydrogen bonds are consistent with the crystallographic evidence for the presence of C–H \cdots O hydrogen bonds.²⁸ It is worthwhile to note that the C–H \cdots O hydrogen bond plays an important role in directing the molecular overlapped packing of acridone. As also found in the crystal packing of *N*-phenylacridone,²⁷ this observation can be served as a guideline in the design of acridone based crystalline materials and other analogous molecules, such as 5-oxophenothiazine and 5,5-dioxophenothiazine.

The influence of the substituents on the electronic properties of acridone derivatives was investigated by the density functional theory (DFT) calculations at B3LYP/6-311+G(2d,p) level of theory *in vacuo* (Fig. 2).²⁹ The LUMOs are located at the acridone moiety with the energy levels in the range 1.78–1.86 eV. The distributions of HOMOs are substituent dependent. With the methoxyphenyl as the substituent, the HOMO mainly occupies the acridone backbone in **2a** with the energy level of –5.81 eV. However, the HOMO locations of **2b** and **2c** are at the pending triphenylamine, which is separated from the LUMO positions and is different from the previously reported donor–acceptor system with amine connecting to the phenyl ring of acridone, in which the HOMO spreads over the whole molecule.¹² The HOMO energy level of **2b** is elevated to –5.36 eV due to the influence of the electron donating dimethoxyphenylamine. The HOMO energy level of **2c** decreases to –5.71 eV, and no HOMO is observed in the acridone moiety, attributable to the extended conjugation of biphenyl.

The redox properties of **2a**–**2c** were studied by measuring cyclic voltammetry (CV) in dichloromethane for oxidation and in THF for reduction. An irreversible oxidation wave at $E_{1/2} = 1.11$ V and a reversible reduction wave at $E_{1/2} = -2.57$ V are observed for **2a** (Table 1, ESI Fig. S24†). However, a reversible

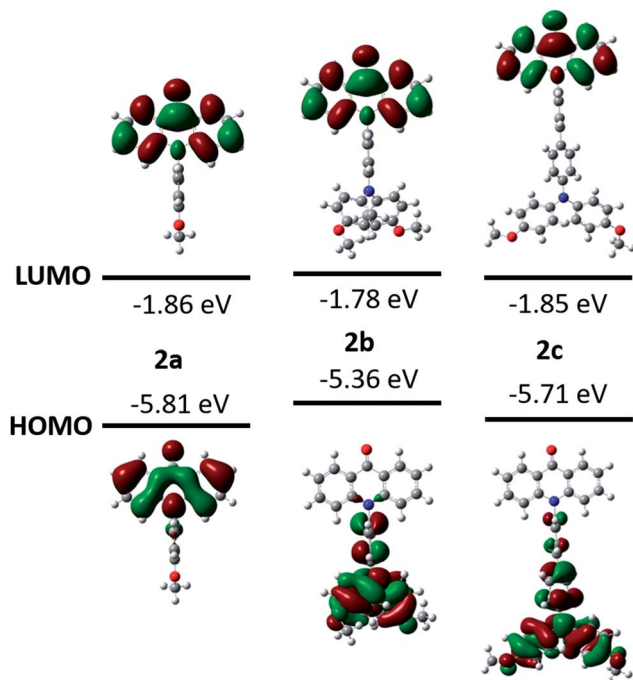


Fig. 2 DFT calculations of the molecular frontier orbitals and energy levels of acridone derivatives.

and an irreversible oxidation waves are found for **2b** and **2c**. The reversible oxidation wave with smaller oxidative potential should originate from the oxidation of triphenylamine, which possesses electron-rich amine with lone pair electrons on the nitrogen atom, thus making the oxidation easier and rising the HOMO energy levels. A reversible reduction wave is seen for **2b** and **2c**, and the half-wave potentials are close to that of **2a**, indicating the similar LUMO energy levels. The electrochemical analysis is in good agreement with the computational results.

The photophysical properties of the compounds **2a–2c** were characterized by UV/vis absorption and fluorescence emission in dichloromethane (Fig. 3). The UV/vis absorption spectra shows that two absorption bands in the long wavelength area are at 376–378 nm and 395–397 nm, which are assigned to the π - π^* transitions.^{2,26} The molar absorbances of **2a** and **2b** are quite close in the band range 395–397 nm, but smaller than that of **2c** due to the extended conjugation. The optical energy gaps estimated from the onsets of the absorptions are 3.05 eV for **2a**,

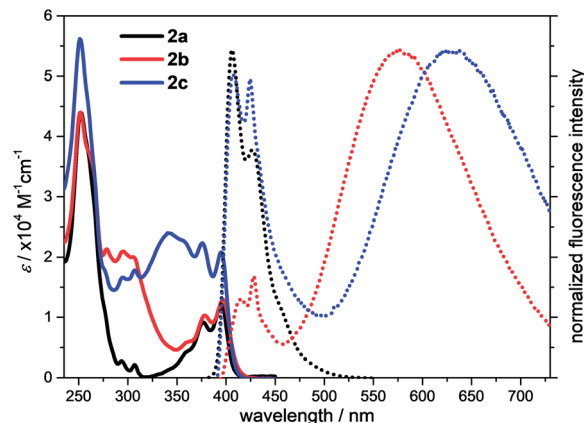


Fig. 3 UV/vis absorption (solid line) and emission (dot line) spectra of **2a**, **2b** and **2c** in dichloromethane at the concentration 10 μ M.

3.01 eV for **2b** and 3.04 eV for **2c**, respectively. The electron transitions were further evaluated by the time-dependent density functional theory (TD-DFT) calculations at the APFD/6-311G+(2d,p) level of theory in dichloromethane solvent (ESI Fig. S29–S31[†]). The absorption band at 395 nm of **2a** is attributed to the HOMO \rightarrow LUMO transition. However, multiple electron transitions are found for the absorptions of **2b** and **2c** at the long wavelength (ESI Tables S7–S9[†]). The UV/vis absorption spectra were also measured in other solvents. Each compound shares similar UV/vis absorption patterns and the shift of band positions is negligible (ESI Fig. S7–S9[†]).

The fluorescence spectra that were measured in dichloromethane at room temperature are shown in Fig. 3. Two emission maxima at 406 nm and 427 nm with an absolute quantum yield of 35% are observed for compound **2a**. The fluorescence time is 1.9 ns and the corresponding radiative and non-radiative rates are $19 \times 10^7 \text{ s}^{-1}$ and $36 \times 10^7 \text{ s}^{-1}$, respectively (ESI Table S4[†]). Interestingly, dual fluorescence emission is detected for **2b** and **2c** in dichloromethane. One emission maximum is in the range 400–464 nm for both of them, which are at the same position to that of **2a** and should originate from the locally excited (LE) state of the acridone moiety. Another emission maximum is very broad and is located at 571 nm for **2b** and 627 nm for **2c**, which should be the results of ICT process between the electron-accepting acridone and the electron-donating triphenylamine. Although the methoxyl group is an

Table 1 Summary of photophysical and electrochemical properties of **2a–2c**

Compd	λ_{max}^a (nm)	$E_{g,\text{opt}}^b$ (eV)	λ_{em}^c (nm)	Φ_{F}^c (%)	λ_{em}^d (nm)	Φ_{F}^d (%)	$E_{\text{ox}1,1/2}^e$ (V)	$E_{\text{red}1,1/2}^f$ (V)	E_{HOMO}^g (eV)	E_{LUMO}^h (eV)	$E_{g,\text{electro}}$ (eV)
2a	395	3.05	406, 427	35	464	13	1.11	−2.57	−5.73	−2.49	3.24
2b	397	3.01	426, 565	1.1	457	17	0.35	−2.55	−5.06	−2.39	2.67
2c	395	3.04	407, 425, 627	1.2	496	2	0.32	−2.50	−5.02	−2.44	2.58

^a Absorption at longest wavelength in dichloromethane at the concentration 10 μ M. ^b Optical energy gap calculated from the absorption onset. ^c Measured in dichloromethane at the concentration 10 μ M, excitation wavelength: 377 nm for **2a**, 379 nm for **2b** and 376 nm for **2c**. ^d Measured in solid state, excitation wavelength: 365 nm for **2a–2c**. ^e Measured in 0.1 M $n\text{-Bu}_4\text{NPF}_6$ in CH_2Cl_2 at room temperature with a scan speed of 0.1 V s^{-1} and ferrocene as internal reference. ^f Measured in THF, the other parameters are same to the measurements in CH_2Cl_2 . ^g $E_{\text{HOMO}} = -(4.8 + E_{\text{ox}1,\text{onset}})$ eV. ^h $E_{\text{LUMO}} = -(4.8 + E_{\text{red}1,\text{onset}})$ eV.

electron-donating group, it is not strong enough to achieve the separation of molecular frontier orbitals, hence only locally excited fluorescence is observed in **2a**. But dimethoxyphenylamine is a stronger electron-donating group and forms the donor–acceptor system with acridone, thus resulting the ICT process. The second emission maximum of **2c** is more red-shifted than that of **2b** due to a longer spacer caused larger dipole moment in the excited state. The absolute quantum yield of **2b** in dichloromethane from the LE state is 1.7%, which is lower than that from the ICT state (3.3%). But the lifetime from the LE state is 3.9 ns, which is longer than that from the ICT state (0.69 ns). Both the radiative and non-radiative rates of **2b** in dichloromethane from the LE state are lower than these from the ICT state. For compound **2c**, the absolute quantum yield (1.7%) and lifetime (4.7 ns) in dichloromethane from the LE state are close to these of **2b**. A quantum yield of 1.2% and lifetime of 4.4 ns for **2c** is found from its ICT state, which leads to a comparable radiative and non-radiative rates to those from the LE state, but smaller than those from the ICT state of **2b**. These results are reasonable considering the relatively longer spacer between the donor and acceptor in **2c**.

The fluorescence property was further investigated by measuring the spectra in different solvents. The emission maximum of compound **2a** shifts from 391 nm in the non-polar solvent cyclohexane with low quantum yield (4.4%) and short lifetime (0.014 ns) to 405 nm in the polar solvent acetonitrile with relatively higher quantum yield (23%) and longer lifetime (2.0 ns). No emissions from the ICT process was observed. But for compound **2b**, dual emissions from both LE and ICT states are observed in other solvents. The emission maximum from the LE state shows a red-shift with the increase of solvent polarity, similar to that of **2a**. No regularity on the positions of emission maximum from the ICT state is found in the non-polar solvent cyclohexane and toluene, but a red shift in the emission from the ICT state with the increase of solvent polarity is observed in the polar solvents. The fluorescence of compound **2c** from the ICT state is gradually isolated from its LE state and the emission is red-shifted from 414 nm in cyclohexane to 627 nm in dichloromethane and cannot be found in the polar acetonitrile. Thus, the emission of acridone–triphenylamine system can be modulated by either adjusting the spacer or changing the polarity of the solvent.

The fluorescence spectra of **2a–2c** were also measured in the solid state (Fig. 4). Compounds **2a** and **2b** are blue fluorescence with the emission maxima at 464 nm and 457 nm, respectively. Whereas compound **2c** demonstrates a weak pale yellow fluorescence with broad emission maxima in the range 458–504 nm. All the emissions in the solid state are red-shifted compared to these from the locally excited states in the solutions due to the close intermolecular contacts caused the excimer coupling.³⁰ The absolute quantum yields are 13% for **2a**, 17% for **2b** and 2% for **2c**, respectively (ESI Table S5†). The loss of emission intensity in solid state is common for the excited states of the aggregates often decay or relax to the ground state in the non-radiative manner.³¹ But compound **2b** in solid state exhibits a much higher quantum yield than that in the solution, demonstrating an aggregation induced enhanced emission

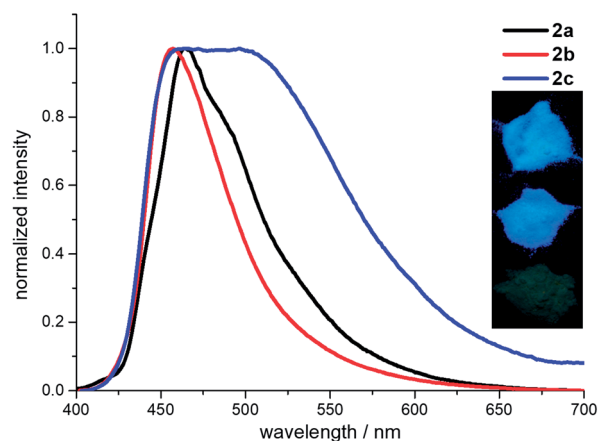


Fig. 4 Fluorescence spectra of **2a–2c** measured in solid state. Inset: the powder emissions (top to down: **2a**, **2b** and **2c**) under 365 nm UV light.

(AIEE). The lifetimes of **2a** and **2b** in the solid state are 3.9 ns and 3.2 ns, respectively, leading to the close radiative ($3.3\text{--}5.3 \times 10^7 \text{ s}^{-1}$) and non-radiative rates ($22.3\text{--}25.9 \times 10^7 \text{ s}^{-1}$). The lifetime of **2c** in the solid state is 37.9 ns, which is longer than those of **2a** and **2b**. The corresponding radiative and non-radiative rates are $0.06 \times 10^7 \text{ s}^{-1}$ and $2.6 \times 10^7 \text{ s}^{-1}$, respectively. The non-radiative rate is about 47 times faster than the radiative rate. Thus, the non-radiative transitions consume most of the energy in the excited states and lead to a weak fluorescence of **2c** in the solid state.

The electron rich triphenylamine is often used to synthesize hole-transporting materials for solar cell.^{32–34} However, it is also an ideal building block in the construction of molecules with AIEE property due to the presence of rotatable C–N bonds.^{35–39} Hence, the photophysical properties of compounds **2a–2c** in the aggregation state was further investigated by measuring their spectra in the water/THF mixture. The absorption maxima at the longest wavelength is red-shifted with the increase of water fraction (ESI Fig. S10–S12†). However, the absorption intensity demonstrates a dramatic loss when water contents are 95% for **2a**, 80% for **2b** and 75% for **2c**, indicating that the aggregation happens at these points. For compounds **2b** and **2c**, the absorption gradually shifts back to its original pattern with the increased water contents.

The fluorescence spectra of **2a** in water/THF demonstrates an interesting variation depending on the water content (ESI Fig. S19†). The emission maxima is red-shifted from 399 nm in pure THF to 409 nm with 10% water fraction accompanied by a rise in the fluorescence intensity due to the water addition caused increase in solvent polarity, which is consistent with the fluorescence spectra measured in different solvents. The fluorescence intensity starts to fall when more water is added and the emission maxima shifts to 425 nm when the water content is 90%. A new emission maximum appears at 431 nm when the water fraction is 95% and reaches its highest intensity with 99% water. This new emission should be the aggregation induced fluorescence, as proofed by the UV/vis absorption analysis. The

average particle size is 337 nm in 99% water (ESI Fig. S25†). The absolute quantum yield is 7.3% in 99% water, which is lower than that in pure THF (10%) and in the solid state (ESI Table S6†). Considering the lifetimes, both the radiative and non-radiative rates gradually decrease from the solution to aggregation state and to the solid state.

Although compound **2b** and **2c** share similar structure, their fluorescence spectra in water/THF are quite different. Compound **2b** in pure THF shows very weak blue fluorescence with an absolute quantum yield of 3.5%. With the increase of water contents in the solvent, a blue fluorescence with the emission maxima at 433 nm starts to appear with 80% water content and reaches its highest intensity (21% quantum yield) in 85% water (Fig. 5). The fluorescence intensity decreases with the increase of water content and the emission maxima is red-shifted to 525 nm. The green fluorescence shows its highest intensity (1.9% quantum yield) in 99% water. This tuneable dual fluorescence emission in aggregation state is rarely reported and it should originate from the different water contents caused variable aggregation states and particle size of compound **2b** in THF.^{40–42} The average particle sizes of compound **2b** in 85% and 95% water are 532 nm and 108 nm, respectively (ESI Fig. S26 and S27†). This reveals that the bigger particle size would lead to a comparable emission to that in its solid state. Indeed, the radiative and non-radiative rates in solid state and in 85% water are quite close to each other, indicating a similar emission manner. The different aggregation state could also be identified by naked eyes when the concentrations of **2b** in 85% and 95% water are increased. Irradiated with a laser pointer, compound **2b** in 85% water is a suspension with scattered light beam due to the big particle size, whereas it is

a sol in 95% water without light scattering. The emission decay of **2b** in 85% water can be fitted in a double-exponential manner with a lifetime of 3.4 ns, whereas the lifetime of **2b** in 95% water is much longer (89 ns) with quadruple-exponential fitting, unravelling the different decay pathway depending on the aggregation state.

Compound **2c** in pure THF presents a bluish green fluorescence with the emission maxima at 473 nm and an absolute quantum yield of 10% (ESI Fig. S22†). The emission intensity reduces due to the increased solvent polarity when water is added. With the increase of water content, a weak yellow fluorescence appears in 85% water, indicating the aggregation induced emission, which is consistent with the results of UV/vis absorption. Compound **2c** gives the strongest yellow fluorescence in 90% water with the emission maxima at 538 nm and an absolute quantum yield of 1.5%, but less than that in pure THF. Compound **2c** in 90% water is a sol with an average particle size of 80 nm, smaller than that of **2b** in 95% water (ESI Fig. S28†). Similar to the sol state aggregation of **2b**, the emission decay of **2c** in 90% water is fitted in a quadruple-exponential way with a longer lifetime (31.5 ns) than in the solution state (2.9 ns), but shorter than that of **2b**.

It is of interest to note that **2b** and **2c** share similar structure, but demonstrate different luminescence in solution and in solid state. In solution, compound **2b** shows weak fluorescence, but the emission of **2c** is stronger. Compound **2c** possesses more rotatable joints than that of **2b**, thus the intramolecular rotation should not be the main reason of weak fluorescence for **2b**. The lower quantum yield of **2b** should be due to the ICT process. Compound **2b** has a short phenyl spacer, which allows a more efficient ICT process from dimethoxyphenylamine to acridone. The fluorescence spectrum of **2b** also shows the luminescence derived from ICT process is the main fraction in the dual fluorescence emission (Fig. 2). With slightly long spacer biphenyl, the ICT process in **2c** is not that so efficient. Together with the reduced conjugation by the nitrogen atom of acridone, it resulted in an improved locally excited emission with stronger intensity than that of **2b**. In the solid state, compound **2b** shows AIEE phenomenon due to the restricted intramolecular rotation, whereas compound **2c** demonstrates aggregation caused emission quenching. It is found that the acridone part favours the formation of π - π stacking from the crystal structural analysis. The distance of neighbouring acridone facets is 3.54 Å for **2b**, which is farther than that of **2c** (3.42 Å). Moreover, compared to **2c**, the dihedral angles of triphenylamine, the acridone and the pending phenyl of **2b** are larger, which can facilitate the isolation of the molecules from each other, thus minimizing the potential non-radiative transitions and improving the luminescence of **2b** in the solid state. Although the rotation around C–N and C–C bonds in **2c** are restricted in solid state, the tight intermolecular contacts caused the electronic coupling makes itself less emissive. The comparison of radiative and non-radiative rates also revealed that the non-radiative transitions is the main reason in the loss of fluorescence intensity for **2c** in solid state.

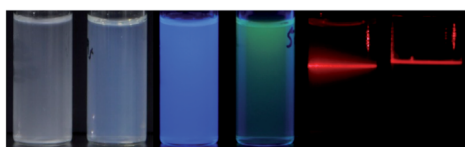
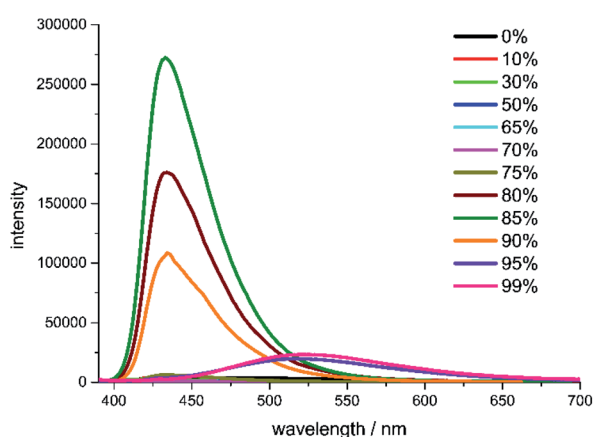


Fig. 5 The fluorescence spectra of **2b** in the THF/water mixtures with different water fractions (concentration: 10 μ M, excitation wavelength: 374 nm). Bottom: the photographs of **2b** in 85% and 95% water (concentration: 50 μ M) under room light (left two), 365 nm UV light (middle two) and irradiation with a laser pointer (right two).

Conclusions

In summary, acridone derivatives with electron-donating groups at the amino position were synthesized and their structural and photophysical properties were investigated. The crystal structural analysis reveals that the acridone moiety tends to form π - π stacking with the assistance of the pending phenyl rings to form C-H \cdots O hydrogen bonds with the carbonyl of acridone, which provides a good strategy in the design of acridone based crystalline materials. Although the strong electron-donating triphenylamine is connected to acridone at the amino position with reduced conjugation, ICT process is observed. Furthermore, the different aggregation states with the variation of water content in THF result in a tuneable blue and green AIEE phenomenon. The size of the spacer between acridone and the pending amine plays an important role in the determination of AIEE or aggregation caused emission quenching. This work will contribute to the design of novel AIEE materials and explore the field of acridone functionalization.

Conflicts of interest

There are no conflicts to declare.

Acknowledgements

We are grateful to the Jiangsu Specially Appointed Professor Plan for financial support.

References

- 1 J. P. Michael, *Nat. Prod. Rep.*, 2008, **25**, 166.
- 2 P. Nikolov, I. Petkova, G. Köhler and S. Stojanov, *J. Mol. Struct.*, 1998, **448**, 247.
- 3 S. E. Garcia-Garrido, C. Caltagirone, M. E. Light and P. A. Gale, *Chem. Commun.*, 2007, 1450.
- 4 I. Móczár, P. Huszthy, A. Mezei, M. Kádár, J. Nyitrai and K. Tóth, *Tetrahedron*, 2010, **66**, 350.
- 5 J. Kaur and P. Singh, *Chem. Commun.*, 2011, **47**, 4472.
- 6 A. Kumar, P. Prasher and P. Singh, *Org. Biomol. Chem.*, 2014, **12**, 3071.
- 7 Y. Xia, W. He, J. Li, L. Zeng, T. Chen, Y. Liao, W. Sun, J. Lan, S. Zhuo, J. Zhang, H. Yang and J. Chen, *Anal. Chem.*, 2019, **91**, 8406.
- 8 B. K. Sharma, A. M. Shaikh, N. Agarwal and R. M. Kamble, *RSC Adv.*, 2016, **6**, 17129.
- 9 P. Pander, A. Swist, R. Motyka, J. Soloduchko, F. B. Dias and P. Data, *J. Mater. Chem. C*, 2018, **6**, 5434.
- 10 Q. T. Siddiqui, A. A. Awasthi, P. Bhui, M. Muneer, K. R. S. Chandrakumar, S. Bose and N. Agarwal, *J. Phys. Chem. C*, 2019, **123**, 1003.
- 11 R. Liu, W. Ding, Q. Zhang, Y. Song and G. Zhang, *ChemistrySelect*, 2019, **4**, 10536.
- 12 K. D. Thériault, C. Radford, M. Parvez, B. Heyne and T. C. Sutherland, *Phys. Chem. Chem. Phys.*, 2015, **17**, 20903.
- 13 R. Liu, G. Zhu, Y. Ji and G. Zhang, *Eur. J. Org. Chem.*, 2019, 3217.
- 14 W. Chen, S. Wang, G. Yang, S. Chen, K. Ye, Z. Hu, Z. Zhang and Y. Wang, *J. Phys. Chem. C*, 2016, **120**, 587.
- 15 T. Suzuki, H. Okada, T. Nakagawa, K. Komatsu, C. Fujimoto, H. Kagi and Y. Matsuo, *Chem. Sci.*, 2018, **9**, 475.
- 16 Y. Matsuo, Y. Wang, H. Ueno, T. Nakagawa and H. Okada, *Angew. Chem., Int. Ed.*, 2019, **58**, 8762.
- 17 D. A. Vezzu, J. C. Deaton, M. Shayeghi, Y. Li and S. Huo, *Org. Lett.*, 2009, **11**, 4310.
- 18 Q. Qi, J. Qian, X. Tan, J. Zhang, L. Wang, B. Xu, B. Zou and W. Tian, *Adv. Funct. Mater.*, 2015, **25**, 4005.
- 19 S. Jiang, J. Wang, Q. Qi, J. Qian, B. Xu, F. Li, Q. Zhou and W. Tian, *Chem. Commun.*, 2019, **55**, 3749.
- 20 Y. Lin, Y. Li and X. Zhan, *Chem. Soc. Rev.*, 2012, **41**, 4245.
- 21 Y. Chen, X. Wan and G. Long, *Acc. Chem. Res.*, 2013, **46**, 2645.
- 22 F. Liu, S. Li, R. Duan, S. Qiu, Y. Yi, S. Wang and X. Zhu, *Sci. China: Chem.*, 2018, **61**, 418.
- 23 C. Zhang and X. Zhu, *Acc. Chem. Res.*, 2017, **50**, 1342.
- 24 M. Kivala and F. Diederich, *Acc. Chem. Res.*, 2009, **42**(2), 235.
- 25 M. Krick, J. J. Holstein, A. Wuttke, R. A. Mata and G. H. Clever, *Eur. J. Org. Chem.*, 2017, 5141.
- 26 R. Liu, H. Gao, L. Zhou, Y. Ji and G. Zhang, *ChemistrySelect*, 2019, **4**, 7797.
- 27 V. E. Zavodnik, L. A. Chetkina and G. A. Val'kova, *Kristallografiya*, 1981, **26**, 392.
- 28 R. Taylor and O. Kennard, *J. Am. Chem. Soc.*, 1982, **104**, 5063.
- 29 M. J. Frisch, G. W. Trucks, H. B. Schlegel, G. E. Scuseria, M. A. Robb, J. R. Cheeseman, G. Scalmani, V. Barone, G. A. Petersson, H. Nakatsuji, X. Li, M. Caricato, A. V. Marenich, J. Bloino, B. G. Janesko, R. Gomperts, B. Mennucci, H. P. Hratchian, J. V. Ortiz, A. F. Izmaylov, J. L. Sonnenberg, D. Williams-Young, F. Ding, F. Lipparini, F. Egidi, J. Goings, B. Peng, A. Petrone, T. Henderson, D. Ranasinghe, V. G. Zakrzewski, J. Gao, N. Rega, G. Zheng, W. Liang, M. Hada, M. Ehara, K. Toyota, R. Fukuda, J. Hasegawa, M. Ishida, T. Nakajima, Y. Honda, O. Kitao, H. Nakai, T. Vreven, K. Throssell, J. A. Montgomery Jr, J. E. Peralta, F. Ogliaro, M. J. Bearpark, J. J. Heyd, E. N. Brothers, K. N. Kudin, V. N. Staroverov, T. A. Keith, R. Kobayashi, J. Normand, K. Raghavachari, A. P. Rendell, J. C. Burant, S. S. Iyengar, J. Tomasi, M. Cossi, J. M. Millam, M. Klene, C. Adamo, R. Cammi, J. W. Ochterski, R. L. Martin, K. Morokuma, O. Farkas, J. B. Foresman and D. J. Fox, *Gaussian 16, Revision A.03*, Gaussian, Inc., Wallingford CT, 2016.
- 30 A. Slodek, A. Maroń, M. Pająk, M. Matussek, I. Grudzkka-Flak, J. G. Małecki, A. Świtlicka, S. Krompiec, W. Danikiewicz, M. Grela, I. Gryca and M. Penkala, *Chem.–Eur. J.*, 2018, **24**, 9622.
- 31 Q. Wu, T. Zhang, Q. Peng, D. Wang and Z. Shuai, *Phys. Chem. Chem. Phys.*, 2014, **16**, 5545.
- 32 K. Rakstys, A. Abate, M. I. Dar, P. Gao, V. Jankauskas, G. Jacopin, E. Kamarauskas, S. Kazim, S. Ahmad, M. Grätzel and M. K. Nazeeruddin, *J. Am. Chem. Soc.*, 2015, **137**, 16172.
- 33 J. Chen, S. Ko, L. Liu, Y. Sheng, H. Han and X. Li, *New J. Chem.*, 2015, **39**, 3736.

- 34 T.-Y. Li, C. Su, S. B. Akula, W.-G. Sun, H.-M. Chien and W.-R. Li, *Org. Lett.*, 2016, **18**, 3386.
- 35 R. Hu, E. Lager, A. Aguilar-Aguilar, J. Liu, J. W. Y. Lam, H. H. Y. Sung, I. D. Williams, Y. Zhong, K. S. Wong, E. Pena-Cabrera and B. Z. Tang, *J. Phys. Chem. C*, 2009, **113**, 15845.
- 36 M. Chen, X. Hu, J. Liu, B. Li, N. L. C. Leung, L. Viglianti, T. S. Cheung, H. H. Y. Sung, R. T. K. Kwok, I. D. Williams, A. Qin, J. W. Y. Lam and B. Z. Tang, *Chem. Sci.*, 2018, **9**, 7829.
- 37 W. Xu, M. M. S. Lee, Z. Zhang, H. H. Y. Sung, I. D. Williams, R. T. K. Kwok, J. W. Y. Lam, D. Wang and B. Z. Tang, *Chem. Sci.*, 2019, **10**, 3494.
- 38 M. Kang, C. Zhou, S. Wu, B. Yu, Z. Zhang, N. Song, M. M. S. Lee, W. Xu, F.-J. Xu, D. Wang, L. Wang and B. Z. Tang, *J. Am. Chem. Soc.*, 2019, **141**, 16781.
- 39 G. Niu, X. Zheng, Z. Zhao, H. Zhang, J. Wang, X. He, Y. Chen, X. Shi, C. Ma, R. T. K. Kwok, J. W. Y. Lam, H. H. Y. Sung, I. D. Williams, K. S. Wong, P. Wang and B. Z. Tang, *J. Am. Chem. Soc.*, 2019, **141**, 15111.
- 40 H. Tong, Y. Hong, Y. Dong, Y. Ren, M. Haussler, J. W. Y. Lam, K. S. Wong and B. Z. Tang, *J. Phys. Chem. B*, 2007, **111**, 2000.
- 41 Z. Luo, X. Yuan, Y. Yu, Q. Zhang, D. T. Leong, J. Y. Lee and J. Xie, *J. Am. Chem. Soc.*, 2012, **134**, 16662.
- 42 J. Liang, Z. Chen, L. Xu, J. Wang, J. Yin, G.-A. Yu, Z.-N. Chen and S. H. Liu, *J. Mater. Chem. C*, 2014, **2**, 2243.